A one-dimensional modeling study of the diurnal cycle in the equatorial Atlantic at the PIRATA buoys during the EGEE-3 campaign

**Malick Wade · Guy Caniaux · Yves duPenhoat ·
Marcus Dengler · Hervé Giordani · Rebecca Hummels**

Abstract A one-dimensional model is used to analyze, at the local scale, the response of the equatorial Atlantic Ocean under different meteorological conditions. The study was performed at the location of three moored buoys of the Pilot Research Moored Array in the Tropical Atlantic located at 10° W, 0° N; 10° W, 6° S; and 10° W, 10° S. During the EGEE-3 (Etude de la circulation océanique et de sa variabilité dans le Golfe de Guinee) campaign of May–June 2006, each buoy was visited for maintenance during 2 days. On board the ship, high-resolution atmospheric parameters were collected, as were profiles of temperature, salinity, and current. These data are used here to initialize, force, and validate a one-dimensional model in order to study the diurnal oceanic mixed-layer variability. It is shown that the diurnal variability of the sea surface temperatures is mainly driven by the solar heat flux. The diurnal response of the near-surface temperatures to daytime heating and nighttime cooling has an amplitude of a few tenths of degree. The computed diurnal heat budget experiences a net warming tendency of 31 and 27 Wm^{-2} at 0° N and 10° S, respectively, and a cooling tendency of 122 Wm^{-2} at 6° S. Both observed and simulated mixed-layer depths experience a jump between the nighttime convection phase and the well-stabilized diurnal water column. Its amplitude changes dramatically depending on the meteorological conditions occurring at the stations and reaches its maximum amplitude (~50 m) at 10° S. At 6° and 10° S, the presence of barrier layers is observed, a feature that is clearer at 10° S. Simulated turbulent kinetic energy (TKE) dissipation rates, compared to independent microstructure measurements, show that the model tracks their diurnal evolution reasonably well. It is also shown that the shear and buoyancy productions and the vertical diffusion of TKE all contribute to the supply of TKE, but the buoyancy production is the main source of TKE during the period of the simulation.

Keywords One-dimensional model · PIRATA buoys ·
Diurnal cycle · Turbulence · Atlantic cold tongue ·
Equatorial Atlantic · Oceanic mixed-layer processes

M. Wade (✉) · G. Caniaux · H. Giordani
Centre National de Recherches Météorologiques,
42 Av. Gustave Coriolis,
31057 Toulouse Cedex, France
e-mail: malick.wade@cnrm.meteo.fr
e-mail: malick172@yahoo.fr

M. Wade · Y. duPenhoat
IRD, LEGOS,
14 avenue Edouard Belin,
31400 Toulouse, France

M. Wade
LPAOSF,
Dakar, Senegal

Y. duPenhoat
Université de Toulouse, UPS/OMP,
31400 Toulouse, France

M. Dengler · R. Hummels
IFM-GEOMAR,
Kiel, Germany

1 Introduction

In this study, we examine the upper eastern equatorial Atlantic (hereafter EEA) diurnal mixed-layer variability during the appearance of the Atlantic cold tongue (ACT). The ACT extends from the African coast to roughly 20° W and reaches its minimum temperature at the equator near

10° W (Carton and Zhou 1997). In the ACT, sea surface temperatures (SSTs) drop relatively fast in spring and early boreal summer by as much as 7°C (Merle et al. 1980; Picaut 1983).

A number of observational (Merle et al. 1980; Foltz et al. 2003) and modeling (Philander and Pacanowski 1986; Yu et al. 2006; Peter et al. 2006) studies have addressed the causes of the seasonal cycle of SSTs in the EEA. They converge to indicate that during ACT formation, the main cooling is due to vertical subsurface processes (vertical advection, mixing, and entrainment), which are nearly balanced by the warming due to atmospheric fluxes, but horizontal advection can also make a significant contribution locally. Off the equator, the SST variability is governed by completely different processes, mainly by atmospheric forcing (Yu et al. 2006; Peter et al. 2006).

However, Foltz et al. (2003) indicate that the seasonal cycle of the mixed-layer heat budget derived from Pilot Research Moored Array in the Tropical Atlantic (PIRATA) buoys is far from being closed, and this prevents the validation of modeled heat budgets. Although these studies help improve our understanding of the physical processes at play while the ACT is building up, the detailed processes of its formation are still poorly understood. This lack of understanding is accentuated by the fact that current climate models are not configured to resolve the diurnal cycle in the upper ocean or the interaction of the ocean and the atmosphere on these timescales. For example, the modulation of the diurnal cycle due to cloudiness is not well known, which limits the heat input at the surface. Moreover, the warming and cooling of SSTs between day and night affect the atmosphere stability and can modulate convection (Leduc-Leballeur et al. 2010). Surface winds prevent stratification and limit the diurnal warming amplitude by mixing the top layers and by increasing the turbulent surface heat fluxes. In equatorial regions, as strong diurnal variations on short-wave radiation are observed, the question is to know whether the stabilizing effect of short-wave radiation and wind-induced mixing combine or compensate each other to affect the diurnal cycle of SSTs. The high temporal resolution data collected during the Analyse Multidisciplinaire de la Mousson Africaine (AMMA)/Etude de la circulation océanique et de sa variabilité dans le Golfe de Guinée (EGEE) programs, which will be discussed further, is thus the opportunity to examine these questions in details.

An outstanding question in the EEA is the impact of turbulent mixing on upper ocean stratification and associated diapycnal heat flux on the mixed-layer heat budget (Foltz et al. 2003; Schmitt et al. 2005). Diapycnal mixing is expected to be elevated in the EEA because of

the presence of the intense vertically sheared system formed by the equatorial undercurrent (EUC) and the south equatorial current (SEC; e.g., as observed at 10° W by Bunge et al. 2007). As the shear is largest in or just below the mixed layer, diapycnal mixing can largely influence SSTs (e.g., Voituriez and Herbland 1977). In fact, the occurrence of Kelvin–Helmholtz instabilities in the upper shear zone of the EUC and associated enhanced diapycnal mixing just below the mixed layer were recently shown by Dengler et al. (2010) from observations collected in September 2005. The strong diapycnal heat flux from the mixed layer into the deep ocean determined in this study was 60 Wm^{-2}, which translates into a cooling of the mixed layer of about 1° per month. Vertical mixing is largely modulated at all timescales by the weakening or strengthening of the trade winds and by the variability of the EUC intensity (Hormann and Brandt 2007).

Furthermore, the EEA is the second most intense oceanic source on earth of CO_2 for the atmosphere after the equatorial Pacific (Takahashi et al. 2009). This source of CO_2 is associated with the equatorial upwelling and brings cold, CO_2-rich waters to the surface. Data collected in the EEA indicate that biogeochemical parameters undergo a clear diurnal cycle (Lefèvre et al. 2008). To understand the physical and biogeochemical processes causing the CO_2 variability, it is necessary to focus on the diurnal timescales in both the oceanic and the atmospheric boundary layers.

To improve understanding of the West African Monsoon, the AMMA program (Redelsperger et al. 2006) was conducted with emphasis on daily-to-interannual time-scales. This program allowed coordinated experiments to be run to document both the oceanic and atmospheric boundary layers in the EEA. The EGEE program (Bourlès et al. 2007), with its strong links with the PIRATA buoy maintenance (Bourlès et al. 2008), was planned to document the oceanic circulation variability. During a research cruise (EGEE-3) from May to June 2006, a measurement program dedicated to the air–sea interface and to the atmosphere was carried out by extending the continental measurement array over the EEA (Janicot et al. 2008).

These campaigns provided an opportunity to acquire high-temporal-resolution data at PIRATA buoy sites, along 10° W (Fig. 1), that can be used to study the diurnal cycle of the mixed layer, the impact of turbulence in the upper layers of the ocean, and the contribution of diurnal temperature variability of the SST.

The investigation was performed along the 10° W section, especially at 10° W, 0° N; 10° W, 6° S; and 10° W, 10° S. The region along 10° W is of interest for three main reasons: (1) it crosses the north to south extension of the ACT; (2) the ACT

Fig. 1 Mean sea surface temperatures (°C) in the eastern equatorial Atlantic during the first 10 days of June 2006 (source: TMI-AMSRE analyses). The three PIRATA buoy stations along 10° W are shown as *blue stars*. The ship's trajectory (*thick line*) is also indicated
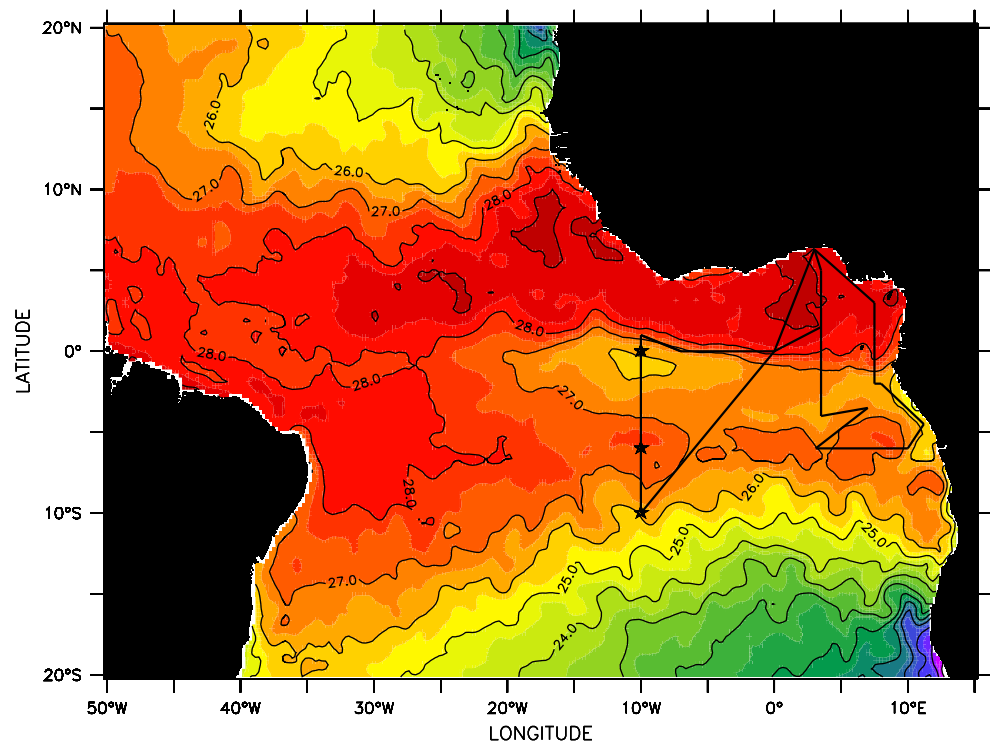
generally appears at 10° W; and (3) the cooling of the ACT is maximum at this location (Caniaux et al. 2010).

The objective of this study was to investigate at short timescales (no more than two diurnal cycles) the contribution of high temporal surface forcing in the vertical ocean structure near the surface and to diagnose how the supply of energy dissipates in the vertical. This approach is easier to perform with a one-dimensional model than a three-dimensional model. Thus, horizontal advection effects, which may affect the stability of the layer, are not taken into account in this study. This can be justified in the tropics because horizontal SST gradients are rather weak (see, e.g., Bernie et al. 2005). The horizontal advection thus modifies the SST mostly at longer timescales (Cronin and McPhaden 1997).

We then utilize a version of the one-dimensional vertical mixing model developed by Gaspar et al. (1990) (hereafter G90) to diagnose the upper ocean diurnal variability in key points in the eastern equatorial Atlantic. This model is used because it has been tested in very different meteorological conditions at the PAPA station and the Long-Term Upper Ocean Study site, where it successfully tracked the evolution of oceanic vertical mixing. Dourado and Caniaux (2004) also used this model to analyze the variability of the upper layer in the equatorial Atlantic; the model reproduces the main features of the upper layer reasonably well. The use of a one-dimensional model is also motivated by the fact that the whole upper vertical ocean structure is retrieved and it allows doing a large number of sensitivity experiments.

The paper is organized as follows. Section 2 describes the regional settings as well as the surface forcing and fluxes, the mean property model, the turbulence closure scheme, and heat and turbulent kinetic energy (TKE) budget techniques. In Section 3, the main results are presented. In Section 4, differences in mixed-layer thicknesses and dissipation rates at stations are discussed.

2 Materials and methods

2.1 Description of field site

In the region of study, the mean oceanic circulation is marked by the presence of a system of intense zonal currents, including the eastward-flowing EUC and the westward-flowing SEC. At 10° W, the EUC extends from about 2° N and 2° S. It has a clearly pronounced core characterized by strong velocities of above 1 m s^{-1} near 70-m depth (Kolodziejczyk et al. 2009). In the late boreal summer and early fall, the core is located at shallower depths than during the rest of the year, more or less following the vertical migration of the thermocline (e.g., Stramma and Schott 1999; Kolodziejczyk et al. 2009). The SEC is composed of two branches, the northern south equatorial current (nSEC) and the central south equatorial current (cSEC). South of 2° S, two eastward-flowing currents are present: the south equatorial undercurrent (SEUC) and the very weak south equatorial countercurrent (SECC). At 10° W, the SEUC is present between about 4° S and 6° S and extends from 50-m depth

to at least 400-m depth. Its core is found between 100 and 150 m, having maximum velocities between 0.30 and 0.40 ms^{-1} (Stramma et al. 2003; Kolodziejczyk et al. 2009).

Another feature of the EEA is the very shallow mixed-layer depth (MLD). Most of the year, the MLD ranges between 15 and 20 m and reaches a maximum depth of some of 30–40 m in the boreal autumn.

The atmospheric circulation in the EEA is dominated by the presence of the ITCZ. During its seasonal progression to the north, the southeastern trade winds intensify in boreal spring and summer. The intensification of the trade wind leads to increased Ekman divergence and creates the ACT south of the equator (Philander 1990). Recently, it has been shown that vertical velocities induced by the strengthening of the current shear between the SEC and the EUC during the boreal summer period also contribute to the formation of the ACT (Giordani and Caniaux 2010). Likewise, remote wind forcing in the western equatorial basin, which induces a shallower thermocline in the EEA through excitation of equatorial Kelvin waves, contributes to eastern equatorial SST cooling (Adamec and O'Brien 1978; Moore et al. 1978; McCreary et al. 1984).

2.2 Surface forcing and fluxes

During the EGEE program (Bourlès et al. 2007), six cruises were conducted in the EEA from 2005 to 2007. Here, we use a dataset acquired during one of these cruises (EGEE-3) that was carried out on the R/V L'Atalante in May–June 2006. This cruise was mainly for the mainte-nance of the PIRATA buoys at 10° W, and en route, hydrological and current measurements were recorded in the upper layers. SST and sea surface salinity were continuously measured with a thermosalinograph (TSG) and the upper ocean currents with a shipboard acoustic Doppler current profiler (ADCP). Atmospheric parameters (including atmospheric pressure, air temperature, relative humidity, wind velocity, and long-wave and short-wave radiations) were acquired with equipment on a mast installed on the foredeck of the ship (Weill et al. 2003). Moreover, atmospheric and oceanic microstructure measure-ments were coordinated along repeated short sections around the PIRATA buoys (Fig. 1), facing the wind while cruising at low speeds in order to achieve optimal conditions for sampling the atmospheric turbulence (Bourras et al. 2009). Oceanic microstructure measurements were recorded using a loosely tethered profiler manufactured by Sea & Sun Technology (Prandke and Stips 1998). The profiler was configured to sink at a speed of 0.6 ms^{-1} and the casts were terminated at a depth of about 200 m.

Figure 2 shows the vertical profiles of zonal and meridional currents at the stations. At 0° N, the current associated with the EUC peaks at 0.8 ms^{-1} at around 50-m

depth. At 6° S, the westward flow associated with the cSEC is <0.2 ms^{-1}. At 10° S, the eastward flow which is associated to the SECC is <0.2 ms^{-1}. During the campaign, trade winds blew from the south to the southeast. At 0° N, their intensity varied from 4 to 8 ms^{-1} (Fig. 3), and the relative humidity was observed to vary from 78% to 86% (Fig. 4). At 6° S, strong and mostly constant winds of about 8 ms^{-1} were observed. At 10-h UTC, stronger winds of about 12 ms^{-1} were present, while the corresponding humidity was 58–70%. At 10° S, winds remained nearly constant at about 7 ms^{-1} and then declined gradually to a minimum of 2 ms^{-1} at 15-h UTC. The relative humidity ranged from 62% to 70%. No rain was recorded along the 10° W section during the campaign.

To accurately simulate the upper ocean diurnal mixed-layer variations, a wide range of surface flux bulk formula-tions (Smith 1980; DeCosmo et al. 1996; Anderson 1993; Fairall et al. 2003; Persson et al. 2005) were tested in order to minimize the errors due to the turbulent heat fluxes. Data used for the surface forcing (the atmospheric parameters, the SSTs, and the radiative heat fluxes) were provided by the instrumented mast. The turbulent fluxes were calculated from the SSTs, the atmospheric pressure, the air tempera-ture and relative humidity, and the wind velocity through the different bulk flux algorithms used by using the following expressions:

$$\tau = \rho_a C_{\mathrm{d}10n} U_{10n} \mathrm{U}_{10n} \qquad (1)$$

$$Q_s = \rho_a C_{pa} C_{\mathrm{h}10n} U_{10n} \Delta T_{10n} \qquad (2)$$

$$Q_L = \rho_a L_{va} C_{\mathrm{e}10n} U_{10n} \Delta q_{10n} \qquad (3)$$

where ρ_a is the air density, C_{pa} the heat capacity of air, L_{va} the latent heat of vaporization, C_{10n} the drag coefficient, $C_{\mathrm{h}10n}$ the sensible heat flux exchange coefficient, $C_{\mathrm{e}10n}$ the latent heat flux exchange coefficient, U_{10n} the neutral equivalent wind speed at 10 m, ΔT_{10n} the difference between the 10-m and surface temperatures, and Δq_{10n} the difference between the 10-m and the surface specific humidity. These data were acquired every 0.1 s, at a rate greater than the time step of the model. They were averaged over 10 min to calculate the turbulent fluxes to force the model.

Table 2 shows the latent heat flux, the sensible heat flux, and the wind stress computed from the different bulk algorithms cited above. Practically, the main discrepancy appears in the latent heat flux. The latent heat flux computed from Anderson's (1993) parameterization is systematically lower than those reported by Persson et al. (2005), Smith (1980), and Fairall et al. (2003) at all the locations. For instance, the difference between latent heat flux computed with the formulations of Anderson (1993) and Fairall et al.

Fig. 2 Zonal (*black*) and meridional (*red*) ADCP velocities (ms^{-1}) at 0° N (*top*), 6° S (*middle*), and 10° S (*bottom*) used for initializing the model
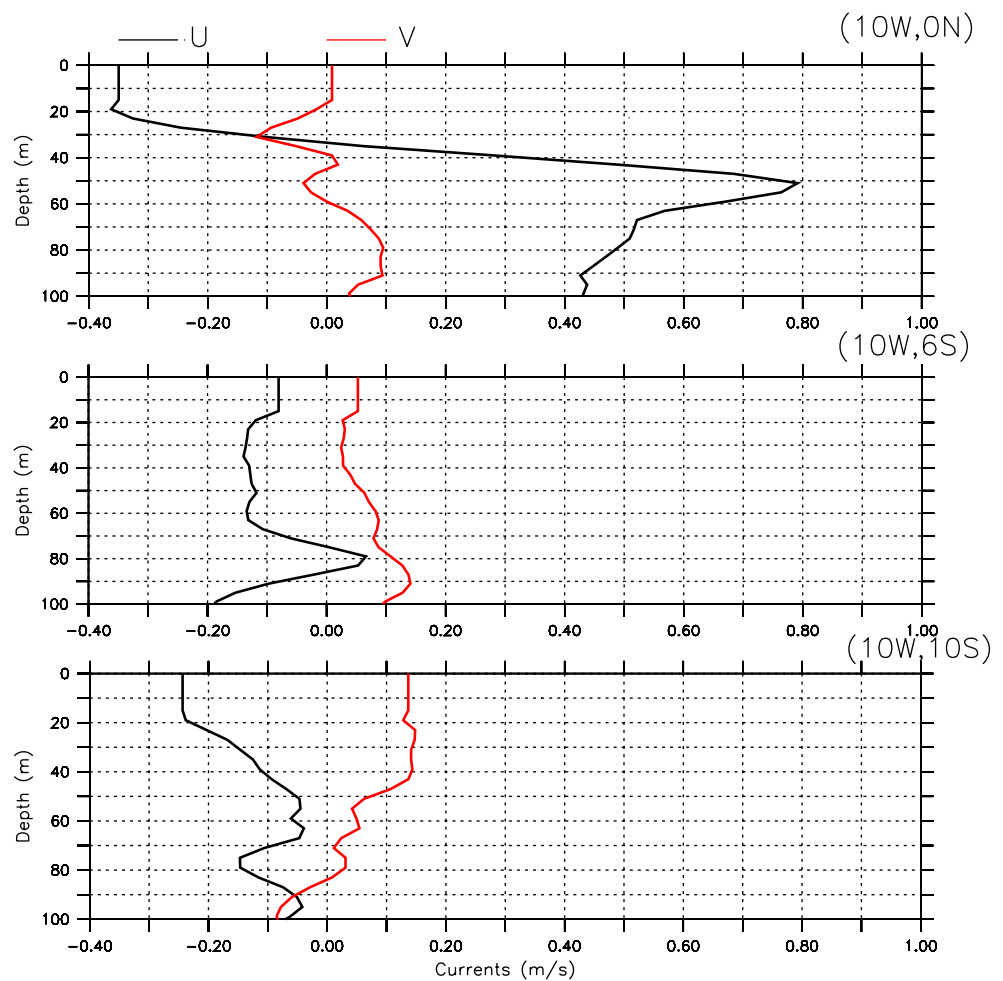
(2003) are −16.1, −45.4, and −34.2 Wm^{-2} at 0° N, 6° S, and 10° S, respectively. At the end of the simulations, these different parameterizations led to SST differences of the order of 0.02°C (i.e., one tenth the amplitude of a diurnal cycle; see Section 2.6 for the sensitivity of the simulation to the different parameterizations).

As expected in this region, the major components of the net heat flux are the incoming solar radiation and the latent heat flux (Fig. 5), while the sensible heat flux and the long-wave radiation have much lower magnitudes. At the three stations, the solar heat flux reached a daily maximum of about 800–900 Wm^{-2}, while the non-solar flux (sum of the latent heat, sensible heat, and infrared heat flux) computed with the parameterizations of Smith (1980) and DeCosmo et al. (1996) varies between −100 and −300 Wm^{-2} according to the station. Note that the convention used in this paper is that positive (negative) heat fluxes indicate warming (cooling) of the ocean. An average over a 24-h period of the net heat flux based on the parameterizations of Smith (1980) and DeCosmo et al. (1996) is 31 Wm^{-2} at 0° N, −122 Wm^{-2} at 6° S, and 27 Wm^{-2} at 10° S. These values reflect the high intraseasonal variability of the winds in this region during ACT development (Marin et al. 2009).

2.3 Mean property model

The model used is a version of the one-dimensional model developed by G90 and improved by Josse (1999). In this model, the conservation laws for the temperature (T), salinity (S), and horizontal components of the velocity (U, V) are written as:

$$\frac{\partial T}{\partial t} = \frac{F_{sol}}{\rho_0 c_p} \frac{\partial I(z)}{\partial z} - \frac{\partial}{\partial z}\left(\overline{T'w'}\right) - w\frac{\partial T}{\partial z} \qquad (4)$$
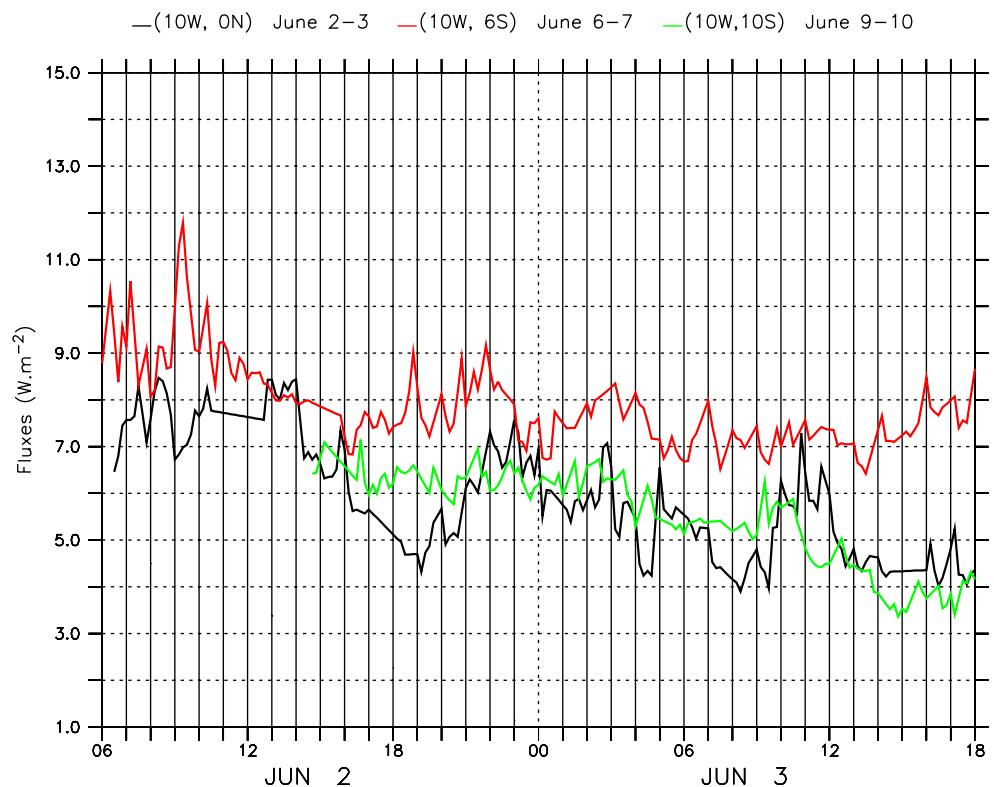
$$\frac{\partial S}{\partial t} = -\frac{\partial}{\partial z}\left(\overline{S'w'}\right) - w\frac{\partial S}{\partial z} \qquad (5)$$

$$\frac{\partial U}{\partial t} = fV - \frac{\partial(\overline{U'w'})}{\partial z} \qquad (6)$$

$$\frac{\partial V}{\partial t} = -fU - \frac{\partial(\overline{V'w'})}{\partial z} \qquad (7)$$

where w is the vertical velocity and f is the Coriolis parameter. The prime operator applied to each variable

represents its turbulent fluctuations and the overbar denotes
a time average. ρ_0 and c_p are the reference density at the sea
surface and the specific heat of seawater, respectively. $I(z)$
is the fraction of F_{sol} (the solar irradiance at the surface)
that penetrates to the depth z, which is parameterized by
(Paulson and Simpson 1977):

$$I(z) = R.e^{-z/D_1} + (1 - R).e^{-z/D_2} \qquad (8)$$

where R denotes the partition parameter of the wavebands
into red- and infrared- and into blue-green light $(1 - R)$,
with attenuation lengths D_1 and D_2, respectively. To take
the effect of upwelling/downwelling at stations into account,
the mean vertical velocity w in Eq. 4 and 5 is estimated
from CTD measurements. This estimation is based on the
assumption that the vertical displacement between two
CTD profiles of an isotherm in the thermocline is due to the
effect of upwelling/downwelling, so that $w = \frac{\Delta H}{\Delta t}$, where H
represents the vertical displacement of the isotherm and Δt
is the time between the two profiles. A similar procedure
was used by Schudlich and Price (1986) and Sprintall and
McPhaden (1994). It is, however, difficult to choose the
appropriate isotherm because its choice is somewhat
arbitrary. Thus, the vertical displacement of the mean
isotherm, which is estimated by averaging all isotherms in
the thermocline, is used to calculate the mean vertical
velocity at each location. By this method, mean vertical
velocities of 0.69 mday^{-1} at 0° N, 0.08 mday^{-1} at 6° S, and

0.1 mday^{-1} at 10° S were estimated from the initial and the
final CTD casts. The turbulent surface fluxes are specified
as follows:

$$-\rho_0 c_p \overline{(T'w')}_0 = F_{nsol} = Q_S + Q_L + F_{ir} \qquad (9)$$

$$-\rho_0 c_p \overline{(S'w')}_0 = E - P \qquad (10)$$

$$-\rho_0 \overline{(U'w')}_0 = \tau_x \qquad (11)$$

$$-\rho_0 \overline{(V'w')}_0 = \tau_y \qquad (12)$$

where F_{nsol} is the "non-solar" surface heat flux (i.e., the
sum of the sensible (Q_S), the latent (Q_L), and the net
infrared (F_{ir}) heat fluxes), whereas $\vec{\tau} = (\tau_x, \tau_y)$ is the
surface wind stress. In Eqs. 4 to 7, the assumption that
turbulent diffusion is down-gradient, depending linearly on
the local property gradient, with appropriate eddy diffusiv-
ity K_X is made:

$$\overline{X'w'} = -K_X \frac{\partial X}{\partial z} \qquad (13)$$

where X stands for momentum U, V and scalar variables T and
S. In the model, the water density is calculated from a linear
version of the equation of state $\rho = \rho_0[1 - \alpha(T - T_0) +$

Fig. 4 Time series of the relative humidity (%) at 0° N (*top*), 6° S (*middle*), and 10° S (*bottom*)
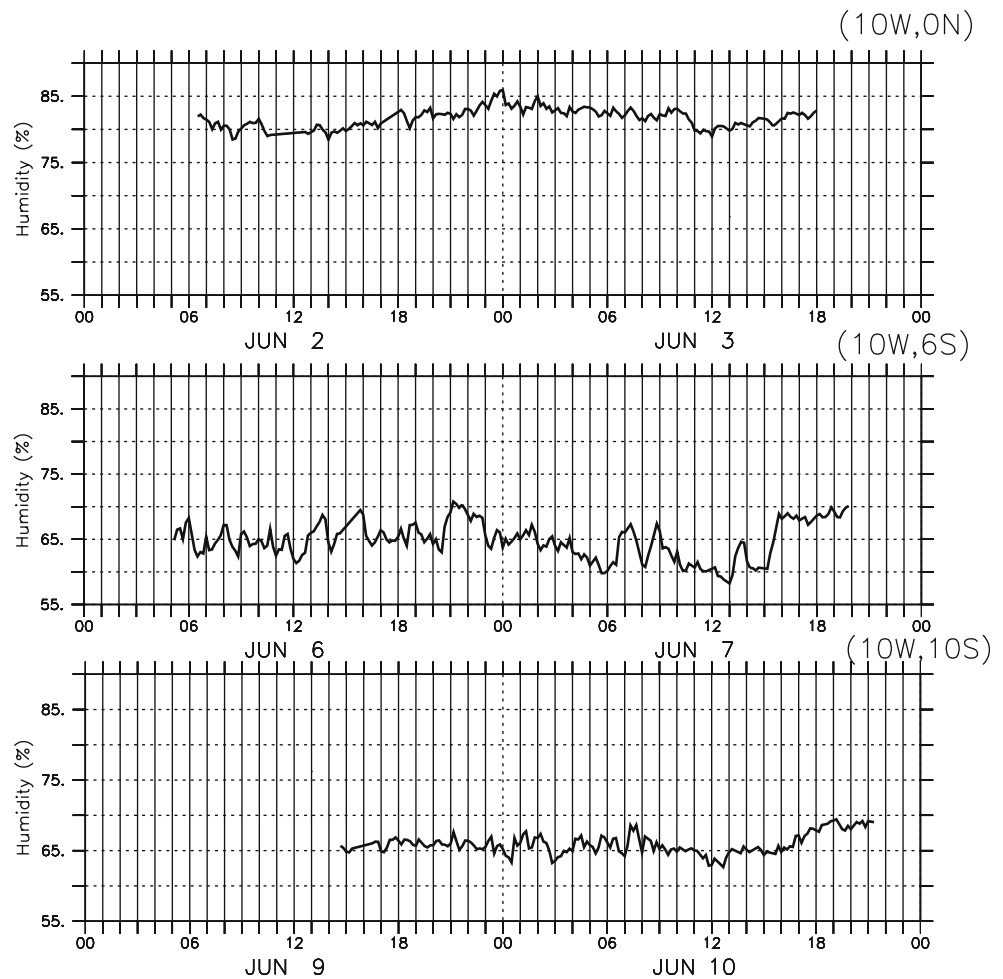
$\beta(S - S_0)]$, where α and β are the thermal and haline expansion coefficients and T_0 and S_0 the reference temperature and salinity contraction, respectively.

The vertical resolution of the model is set to 1 m at a maximum depth of 100 m. The time step is 10 min. The model is initialized with observed temperature and salinity profiles from CTD casts and with observed currents measured by ADCP. At stations, the first CTD cast is used to initialize the model and the last CTD cast as validation.

2.4 Turbulence model

In the model, the turbulence is based on the parameterization developed by Bougeault and Lacarrère (1989) for atmospheric models and adapted to oceanic simulations by G90. This parameterization consists in relating the diffusion coefficient K_X (Eq. 13) to the local TKE (m²s^{-2}, i.e., $e = (u'^2 + v'^2 + w'^2)/2$) with a mixing length scale l_k determined from simple physical considerations and a calibration constant c_k (0.1 in G90):

$$K_X = c_K l_K \overline{e}^{1/2}. \tag{14}$$

To close the system of equations, the TKE equation is given by:

$$\frac{\partial \overline{e}}{\partial t} = -\frac{\partial}{\partial z}\left(\overline{e'w'} + \frac{\overline{p'w'}}{\rho_0}\right) - \left(\overline{u'w'}\frac{\partial U}{\partial z} + \overline{v'w'}\frac{\partial V}{\partial z}\right) + \overline{b'w'} - \varepsilon \tag{15}$$

where p and ε stand for pressure and local dissipation, respectively. $b = g(\rho - \rho_0)/\rho_0$ is the local buoyancy with ρ the density. The concept of turbulent diffusion (Eq. 14) is also used to parameterize the sum of the vertical flux of TKE and the presso-correlation term in Eq. 15, such that:

$$-\left(\overline{e'w'} + \frac{\overline{p'w'}}{\rho_0}\right) = K_e \frac{\partial \overline{e}}{\partial z}. \tag{16}$$

The dissipation term in Eq. 15 is parameterized using the Kolmogorov (1942) theory, i.e., $\varepsilon = c_\varepsilon \overline{e}^{\frac{3}{2}}/l_\varepsilon$, where c_ε is a calibration constant (0.7) and l_ε is a characteristic length of dissipation (Bougeault and Lacarrère 1989).

Below the mixed layer, the turbulence scheme is improved by adding a parameterization of the diapycnal mixing proposed by Large et al. (1994) and Kantha and

Fig. 5 Time series of net heat fluxes (*black*), solar heat fluxes (*green*), and non-solar heat fluxes (*red*) at 0° N (*top*), 6° S (*middle*), and 10° S (*bottom*). Unit: Wm^{-2}
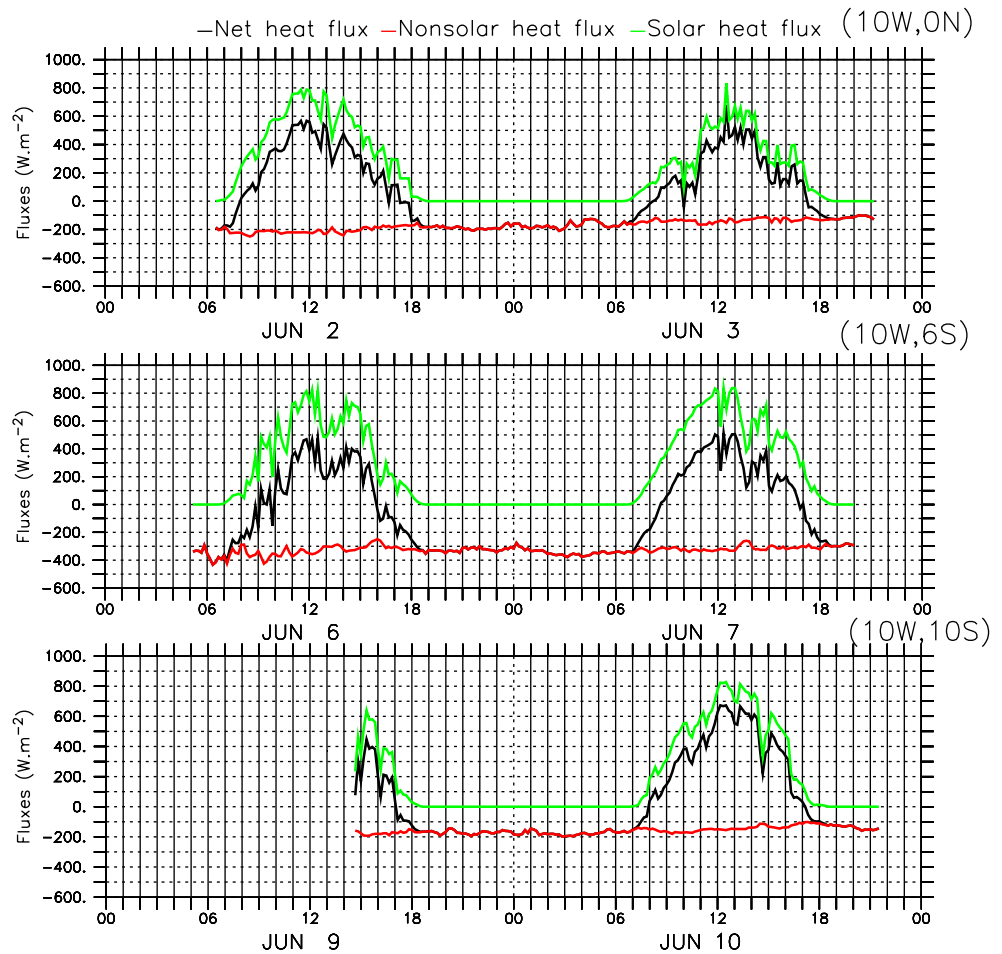
Clayson (1994). This parameterization can largely impact the parameters in the mixed layer (Josse 1999; Dourado and Caniaux 2004). In the model, the mixing coefficients are set to 10^{-4} m²s^{-1} for the temperature and the salinity and to 10^{-5} m²s^{-1} for the momentum (Large et al. 1994).

2.5 Heat and TKE budget techniques

To investigate the processes that control the SST and turbulence, we consider the heat and TKE budget equations in the mixed layer. For this, the temperature and TKE equations (respectively Eqs. 4 and 15) are vertically integrated from the base of the MLD ($-h$) to the sea surface. For the temperature, we obtain (Caniaux and Planton 1998):

$$\rho_0 c_p h \frac{\partial \langle T \rangle}{\partial t} = F_{sol}(1 - I(-h)) + F_{nsol} \qquad (17)$$
$$- \rho_0 c_p \left[\frac{\partial h}{\partial t} + w(-h) \right]$$
$$(\langle T \rangle - T(-h)) + \rho_0 c_p \overline{w'T'}(-h)$$

where $\langle T \rangle = \frac{1}{h} \int\limits_{-h}^{0} T dz$. The first term of the right-hand side of Eq. 17 represents the net solar heat flux absorbed in the

mixed layer; the second term is the non-solar heat flux. The third term is the heat flux due to entrainment (including the MLD tendency and the vertical velocity), and the last term is the turbulent heat flux at the base of the mixed layer. This term is estimated as a residue and is calculated as the storage heat term (left-hand side of Eq. 17) minus the terms on the right-hand side.

The TKE budget equation reads:

$$\int\limits_{-h}^{0} \frac{\partial \overline{e}}{\partial t} dz = - \int\limits_{-h}^{0} K_\rho \frac{\partial}{\partial z} \left(\overline{\frac{g(\rho - \rho_0)}{\rho_0}} \right) dz$$
$$+ \int\limits_{-h}^{0} K_m \left(\left(\frac{\partial U}{\partial z} \right)^2 + \left(\frac{\partial V}{\partial z} \right)^2 \right) dz$$
$$- \int\limits_{-h}^{0} \varepsilon dz + \overline{w'e'}(-h) - \overline{w'e'}(0) \qquad (18)$$

The first term of the right-hand side of Eq. 18 represents the work done by the buoyancy force, the second one the shear production, the third one describes the dissipation, and the last term is the vertical diffusion at the mixed-layer base. As for the heat budget, this last term is calculated as a residue.

2.6 Sensitivity experiments

In order to simulate the upper ocean processes realistically and to adjust the simulation to observations, several sensitivity tests were performed. Tests concerned: (1) the turbulent surface fluxes, which were calculated with the four bulk formulae mentioned in Section 2.2; (2) the set of coefficients defining the water turbidity in Eq. 8 by using different Jerlov's optical water types (Table 1); (3) the sensitivity to the diapycnal mixing (activated or not); and (4) the sensitivity to the vertical velocity term in Eqs. 4 and 5 (activated or not).

The tests led us to adopt a reference set of parameters (called the reference run) which was obtained with: (1) the parameterizations of Smith (1980) and DeCosmo et al. (1996); (2) the coefficients $R=0.62$, $D_1=1.5$ m, and $D_2=20$ m for Jerlov's water type at 6° S and 0° N and $R=0.58$, $D_1=0.35$ m, and $D_2=23$ at 10° S, meaning that two distinct water types were sampled; (3) the diapycnal mixing; and (4) the vertical advection, w, being deduced from the CTDs.

The results of the sensitivity tests at 6° S are represented in a Taylor (2001) diagram in Fig. 6. This diagram provides an easy way of presenting results concerning an ensemble of sensitivity tests by comparing several statistics simultaneously: the standard deviation, the correlation, and the centered root-mean-square (rms) errors. For this, the SST series obtained with the reference run is considered (point "A" in Fig. 6). Then, each SST test series obtained from a sensitivity experiment and the reference series provides a statistic, which is reported on a Taylor polar graph as letters "B" to "K" (Fig. 6). The criteria are listed in detail in Tables 3.

It is clear from Fig. 6 that the diapycnal mixing is crucial for the simulation because run "J" (Table 3 and Fig. 6) has a very weak correlation (0.72) and a high rms (0.085°C) compared to the other runs. Tests on the turbidity indicate that for run "B" (very clear waters in Jerlov's classification), the correlation is lower than in simulations "C", "D", "E," and "F", meaning that at 6° S, waters were rather
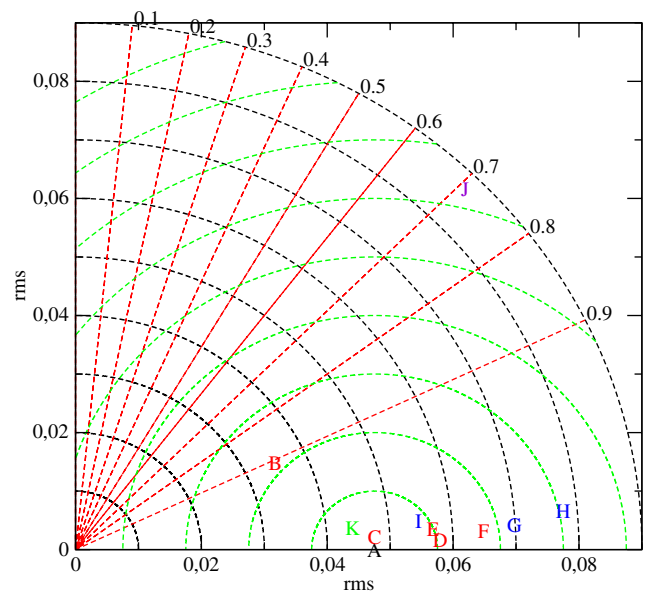
Fig. 6 Taylor's (2001) diagram applied to the sensitivity tests for 11 options defined in Table 3. *Black dashed circles* which are centered on the origin refer to the standard deviation of the reference series (*A*). *Green dashed isolines* centered on the reference series A refer to the centered root mean square difference between the test and reference series. *Dotted red lines* refer to the correlation between the test and reference series. Red labels (*B–F*) refer to turbidity test series; *blue labels* (*G–I*) to turbulent flux parameterization test series; *green label* (*K*) to vertical velocity test; and *violet label* (*J*) to diapycnal mixing test

turbid. Sensitivity tests on flux parameterization ("I", "G", "H") led to higher rms values than simulations on turbidity. The run on the vertical velocity ("K") is highly correlated with the reference run and leads to a similar rms, meaning that less sensitivity is obtained with the vertical velocity than with the other tests. Results at 10° W, 0° N and 10° W, 10° S (not shown) led to the same conclusion. Note that the sensitivity experiments were done only on SSTs. In the following, the reference simulation at the stations is considered and compared to the observations.

3 Results

3.1 Sea surface temperature

Simulated temperatures at stations are compared with TSG and PIRATA buoy data in Fig. 7. Considering the depth (4 m) of the TSG measurements, the simulated temperatures are taken at the same depth and are referred to as SSTs hereafter. The simulated SSTs are in good agreement with the TSG observations since the difference between modeled and observed SSTs is about 0.01°C with standard deviations of 0.015°C. The agreement is also satisfactory when compared with PIRATA buoy data (Fig. 7). At stations, a diurnal cycle of SST is present both

Table 1 Values of the coefficients in the Paulson and Simpson (1977) representation of downward irradiance versus depth for different optical water types

		R	D_1 (m)	D_2 (m)
Type 0		0.74	1.7	16
Jerlov (1968)	Type I	0.58	0.35	23
	Type IA	0.62	0.60	20
	Type IB	0.67	1.0	17
	Type II	0.77	1.5	14
	Type III	0.78	1.4	7.9

Table 2 Values of the latent heat fluxes, sensible heat fluxes (Wm^{-2}), and wind stress (Nm^{-2}) obtained in the three simulations with various turbulent surface flux algorithms

		Smith (1980)	Anderson (1993)	Fairall et al. (2003)	Persson et al. (2005)
Latent heat flux (Wm^{-2})	0° N	−80.0	−95.7	−79.6	−92.7
	6° S	−226.2	−269.6	−224.2	−259.5
	10° S	−154.9	−186.0	−151.8	−179.1
Sensible heat flux (Wm^{-2})	0° N	−3.2	−3.2	−3.2	−3.2
	6° S	−12.3	−12.4	−12.4	−12.9
	10° S	−10.0	−10.2	−10.0	−10.0
Wind stress (Nm^{-2})	0° N	0.041	0.036	0.044	0.044
	6° S	0.078	0.073	0.084	0.086
	10° S	0.037	0.033	0.040	0.040

in TSG data and in the simulations. The amplitude of the diurnal cycle is found to be 0.20°C, 0.12°C, and 0.25°C at 0° N, 6° S, and 10° S, respectively. Note that at 6° S, the amplitude is nearly half that at 0° N and 10° S, a consequence of stronger winds and the negative surface heat flux recorded at this location.

The maximum of daily SSTs occur during the afternoon, between 1400 and 1500 UTC (1300–1400 local time), while the SST minimum occurs between 0800 and 0900 UTC, and again, the model reproduces their occurrence quite well. The occurrence of the minima coincides with a change in sign of the net surface heat flux from negative to positive as heating from surface solar radiation increases relative to cooling from the non-solar flux (Fig. 5). Similarly, the maximum of SST occurs when the net heat flux moves from positive to negative. This moment does not coincide with the maximum solar heat flux, which occurs some hours earlier, usually at 1200 UTC (Fig. 5). Therefore, as the period of the day during which the net heat flux becomes negative is longer than the period during which it is positive (Fig. 5), the cooling of the ocean surface layers lasts longer (15–16 h) than the warming (7–9 h). This is consistent with Schudlich and Price's (1986) results

of a warming time of one fourth of the day and a cooling period of three fourths of a day.

3.2 Vertical profiles of temperature and salinity

Vertical profiles of temperature and salinity (from a Seabird 911 plus system and from temperature and conductivity sensors attached to the microstructure profiler) observed at the end of the stations are compared with the final profiles of the simulation in Fig. 8. The simulated temperature and salinity profiles compare reasonably with observations, both in the mixed layer and in the upper thermocline.

The temperature profiles are well mixed down to 20, 65, and 60 m, respectively, at 0° N, 6° S, and 10° S with a well-defined gradient underneath, which defines the stratified upper thermocline. These depths and the depths of the 20°C isotherm (observed at 50 m at 0° N, 90 m at 6° S, and 100 m at 10° S) are in agreement with meridional sections of temperature showing a classical equatorward shoaling of the thermocline at 10° W (Bourlès et al. 2002; Kolodziejczyk et al. 2009).

In the upper thermocline, vertical displacement of isotherms in observed profiles are clearly visible. These

Table 3 Criteria used to determine the sensitivity tests and to name the runs in Fig. 6

Runs	Parameterizations	Water type	Vertical velocity	Diapycnal mixing
A (reference)	Smith (1980) and DeCosmo et al. (1996)	Type 0	Yes	Yes
B	Smith (1980) and DeCosmo et al. (1996)	Type I	Yes	Yes
C	Smith (1980) and DeCosmo et al. (1996)	Type IA	Yes	Yes
D	Smith (1980) and DeCosmo et al. (1996)	Type IB	Yes	Yes
E	Smith (1980) and DeCosmo et al. (1996)	Type II	Yes	Yes
F	Smith (1980) and DeCosmo et al. (1996)	Type III	Yes	Yes
G	Fairall et al. (2003)	Type 0	Yes	Yes
H	Persson et al. (2005)	Type 0	Yes	Yes
I	Anderson (1993)	Type 0	Yes	Yes
J	Smith (1980) and DeCosmo et al. (1996)	Type 0	Yes	No
K	Smith (1980) and DeCosmo et al. (1996)	Type 0	No	Yes

Fig. 7 Variation of the diurnal
SSTs (°C): simulated (*black*)
and observed (*red*) at 0° N (*top*),
6° S (*middle*), and 10° S
(*bottom*)
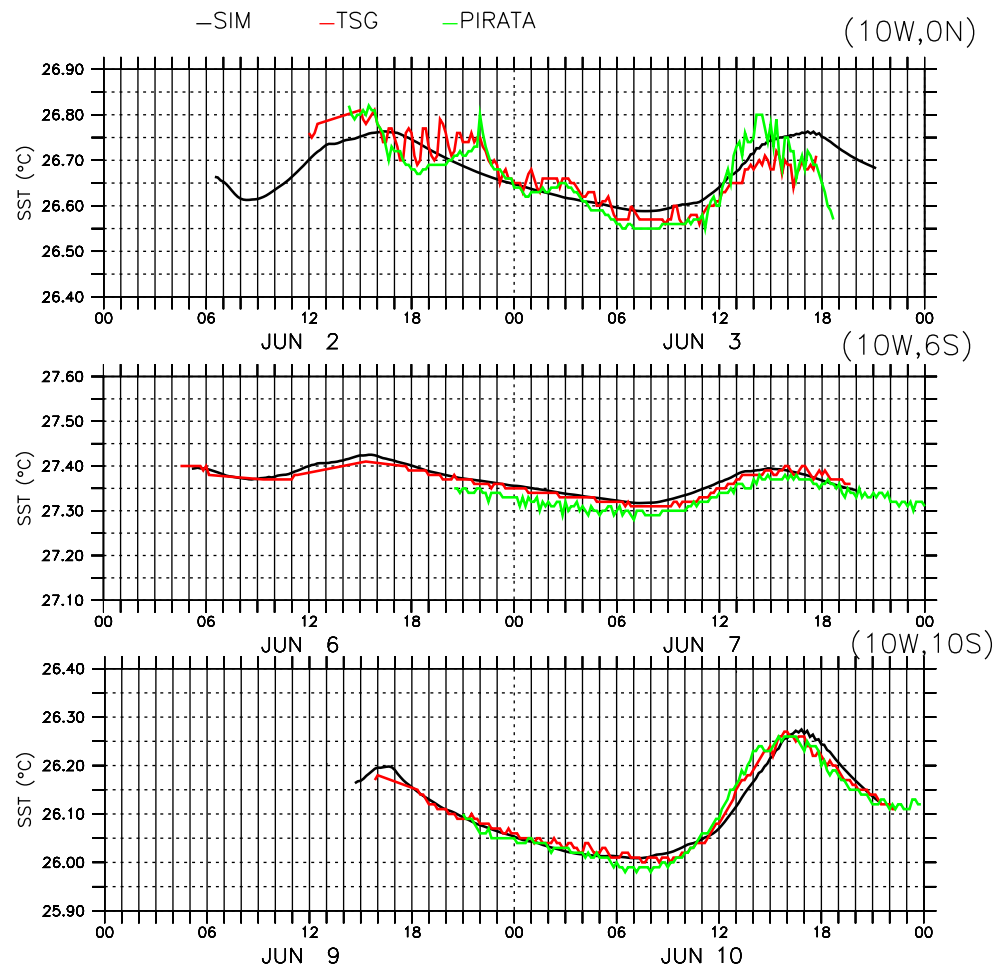
changes reflect the effect of vertical advection, a term
which contributes to the evolution of the profiles in the
stratified water column but only weakly affects the
homogenous mixed layer, which evolves mainly under the
influence of surface heat fluxes.

Distinctive temperature and salinity structures are present
in the initial profiles (Fig. 8), like the strong salinity
maximum present just below the mixed layer at 6° S and
10° S or inside the thermocline at 0° N. These maxima are
associated with the subsurface currents (EUC at 0° N and
SEUC at 6° S; Fig. 2) which advect saline subtropical waters
below the surface layer to the EEA (Bourlès et al. 1999). At
10° S, the salinity maximum present near 50 m, although not
associated with a noticeable current, is less well marked than
at the other latitudes.

In the mixed layer, a meridional salinity gradient of
nearly 1 psu exists between 10° S and the equator. No
similar gradient exists in the mixed-layer temperatures,
which exhibit a slight latitudinal variation with a minimum
of 26°C at 10° S, a maximum of 27°C at 6° S, and a
decrease to near 26.5°C at 0° N, in agreement with Fig. 1.

Observed temperature and salinity profiles show that a
difference of nearly 8 and 15 m exists between the depth of

the (shallower) isohaline and the depth of the (deeper)
isothermal layers at 6° S and 10° S, respectively (Fig. 8).
This difference can be explained by the presence of barrier
layers at these stations (Pailler et al. 1999; Mignot et al.
2007). These authors identified the presence of barrier layers
over several zones in the tropical Atlantic basin, among
them one located on an equatorial band centered at 10° S.

3.3 Mixed layer thickness

Figure 9 displays the observed and simulated MLDs at the
different locations. A temperature criterion with a threshold
of 0.2°C and a reference depth at the surface was chosen to
estimate the MLD. There is relatively good agreement
between the observed and the simulated MLDs. The largest
differences reach nearly 20 m during a relatively short
period of time in the afternoon (between 1300 and 1400
UTC) at 10° S.

Pronounced MLD variations are noted in the observa-
tions and in the simulations. The diurnal range of MLD is 5
and 20 m at 0° N and between 5 and 60 m at 10° S, while
almost no variations are observed at 6° S. The absence of
variations at 6° S is certainly related to stronger winds than
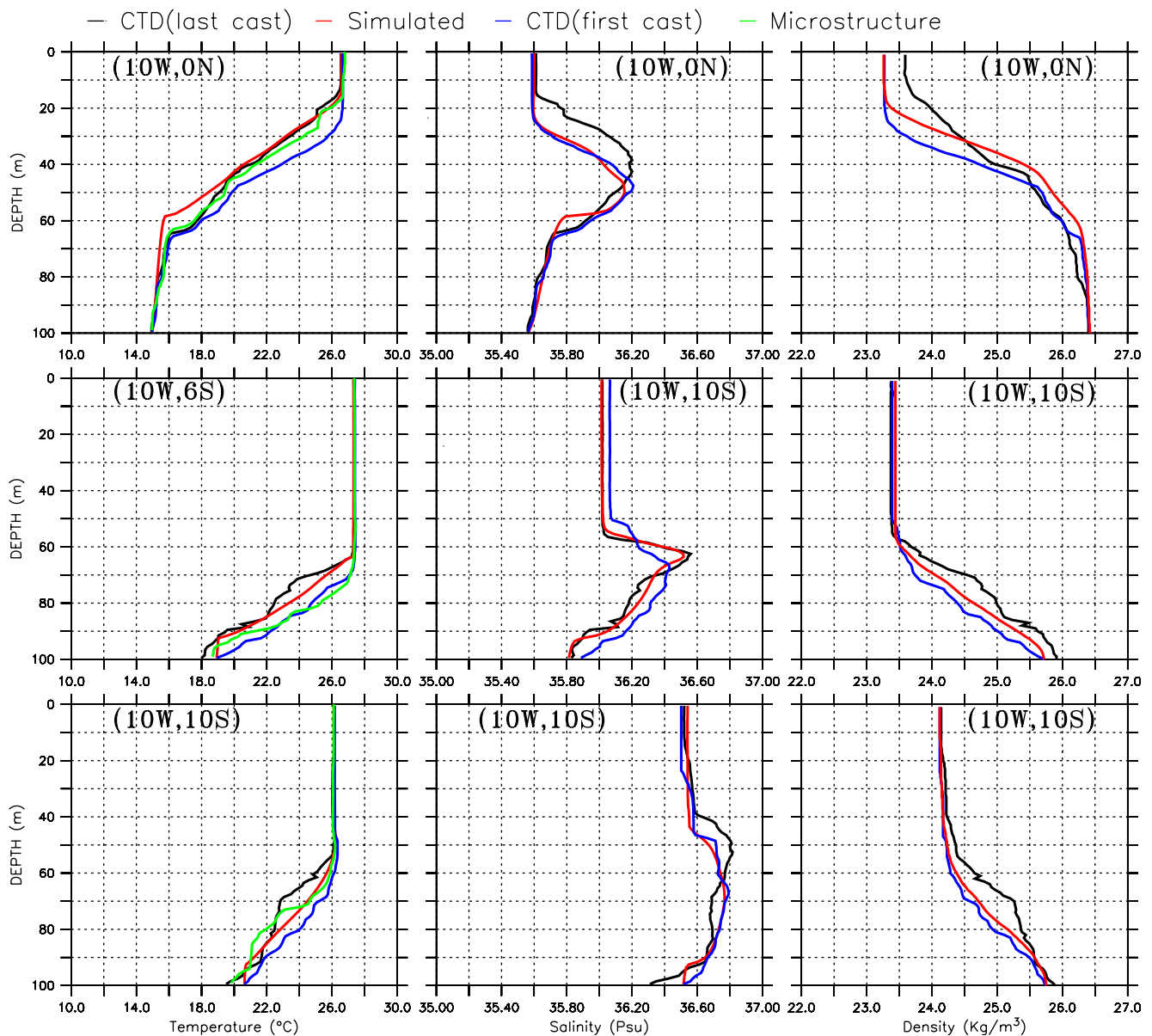
Fig. 8 Vertical profiles of temperature (*left column*) in °C, salinity (*middle column*) in psu, and density (*right column*) in kgm^{-3}: CTD (*first cast in black*), CTD (*last cast in blue*), simulated (*red*), and microstructure (*green*) at 0° N (top), 6° S (middle), and 10° S (bottom)

at other stations (Fig. 5), preventing any diurnal warming that would stratify the upper layers. Here, the absence of a diurnal cycle in MLDs (for the used MLD criteria) suggests the existence of a balance between the effect of the wind stress and the effect the surface net heat flux during the day. If the wind stress exceeds a certain threshold, the diurnal positive net heat flux is unable to stratify the upper layers. On the other hand, it is thought that the wind stress registered at 6° S, added to negative heat flux over 24 h, is not strong enough to deepen MLDs, which finally remain unchanged. According to the data collected at 6° S (see Fig. 3), this threshold is around 6 ms^{-1}. Moreover, it is also

possible that the time period we are looking at is too short to detect any noticeable deepening.

The diurnal cycle of the MLD, well marked at 0° N and very clear at 10° S with an abrupt surfacing at 1200 UTC (amplitude 55 m) exists during a period of 10 h (Fig. 9), between 1100 UTC (i.e., 2 h before the diurnal maximum of the net heat flux; Fig. 5), and near 2100 UTC (i.e., well after the instant at which the net surface heat flux changes from positive to negative; Figs. 5, 9). This abrupt surfacing of the MLD is due to the formation of a thin diurnal thermocline which is destroyed 5 h later. The delay between the instant at which the net heat flux turns positive from its nocturnal to its

Fig. 9 Time series of the simulated (*black*) and observed (*red*) mixed layer depth at 0° N (*top*), 6° S (*middle*), and 10° S (*bottom*)
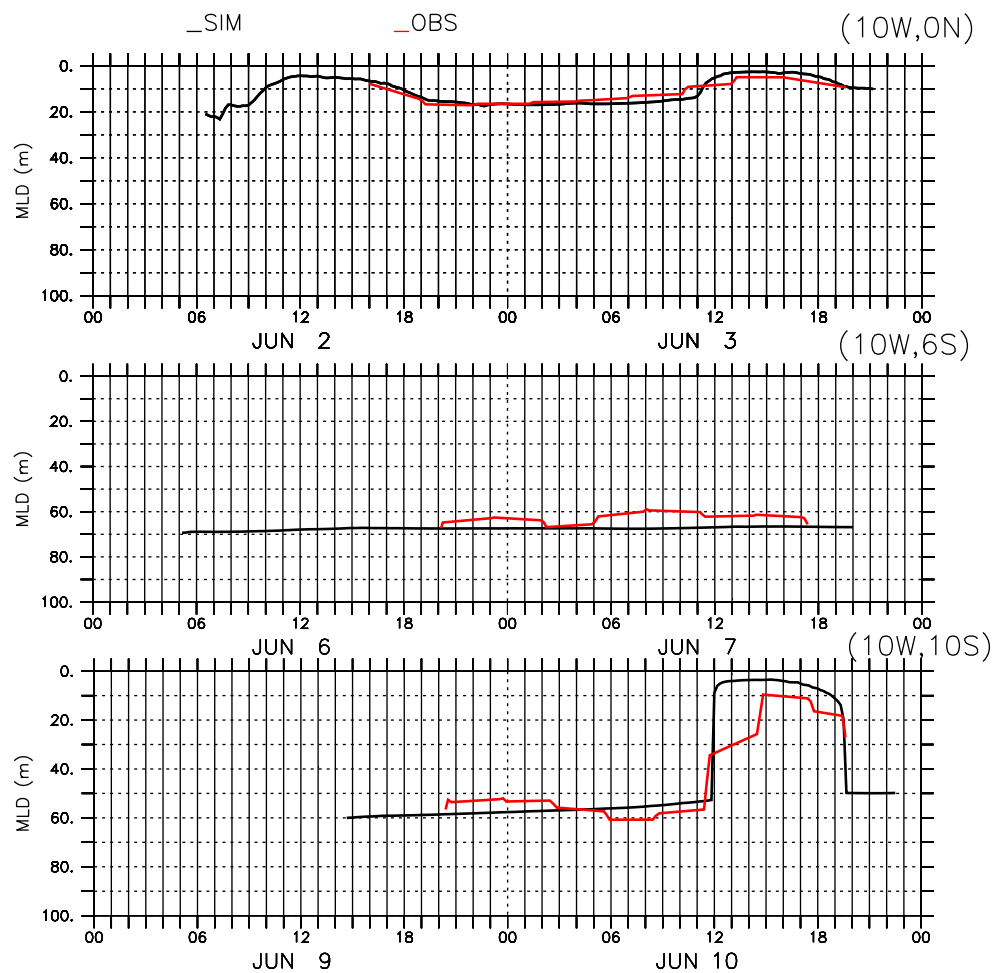
diurnal values and the instant at which the mixed layer shoals is due to the influence of the surface wind stress, which, when strong enough, destroys the quiescent stratification; this situation persists until the net solar radiation is high enough to definitely stratify the top layers.

3.4 Current

Near-surface temperatures and currents relative to 25 m (representative of the shear on this depth) at the various locations are displayed in Fig. 10. At the equator and at 10° S, the net diurnal stratification discussed previously and starting at 1200 UTC is present and is more pronounced at the equator, while at 6° S, no clear stratification is observed. The current relative to 25 m intensifies toward the surface when the diurnal stratification occurs, while at depth, the current diminishes.

A diurnal jet is generated in the top few meters of the mixed layer in the lee of the wind at 0° N and to the left of the wind at 10° S. Its maximum amplitude is reached when the stratification is maximum (few hours after noon). This is due to the fact that most of the wind

stress-generated momentum is trapped within the shallow mixed layer and stratification at the base of this diurnal layer prevents diffusion of the current below. At the equator, the maximum current is 0.11 m s^{-1} at 5-m depth. As the diurnal warm layer cools and vanishes, the diurnal jet vanishes and wind momentum spreads over the entire ML down to the permanent thermocline. Schudlich and Price (1986), in a modeling study, and Cronin and Kessler (2009), on mooring observations, have shown similar results in the Pacific.

3.5 Turbulence

In this section, we compare the dissipation of TKE $\left(\varepsilon = c_\varepsilon \overline{e}^{\frac{3}{2}}/l_\varepsilon\right)$ with dissipation profiles collected during EGEE3. The temporal evolution of the modeled dissipation profiles (Fig. 11) shows a relatively good resemblance to observations concerning both: (1) the order of magnitude of the dissipation with values higher than 10^{-8} W kg^{-1} inside the mixed layer; (2) the decreasing values of the dissipation from the surface, where it reaches its maximum (10^{-6} W kg^{-1}), towards the depths; and (3) their variations during a

Fig. 10 Time–depth sections of temperature in the first 25 m and winds (*blue vectors*) at 10° W, 0° N (*top*), 10° W, 6° S (*middle*), and 10° W, 10° S (*bottom*) during the simulation. Currents relative to 25 m are superimposed (*black vectors*). Vector scales are 0.2 ms^{-1} for the currents and 9 ms^{-1} for the winds
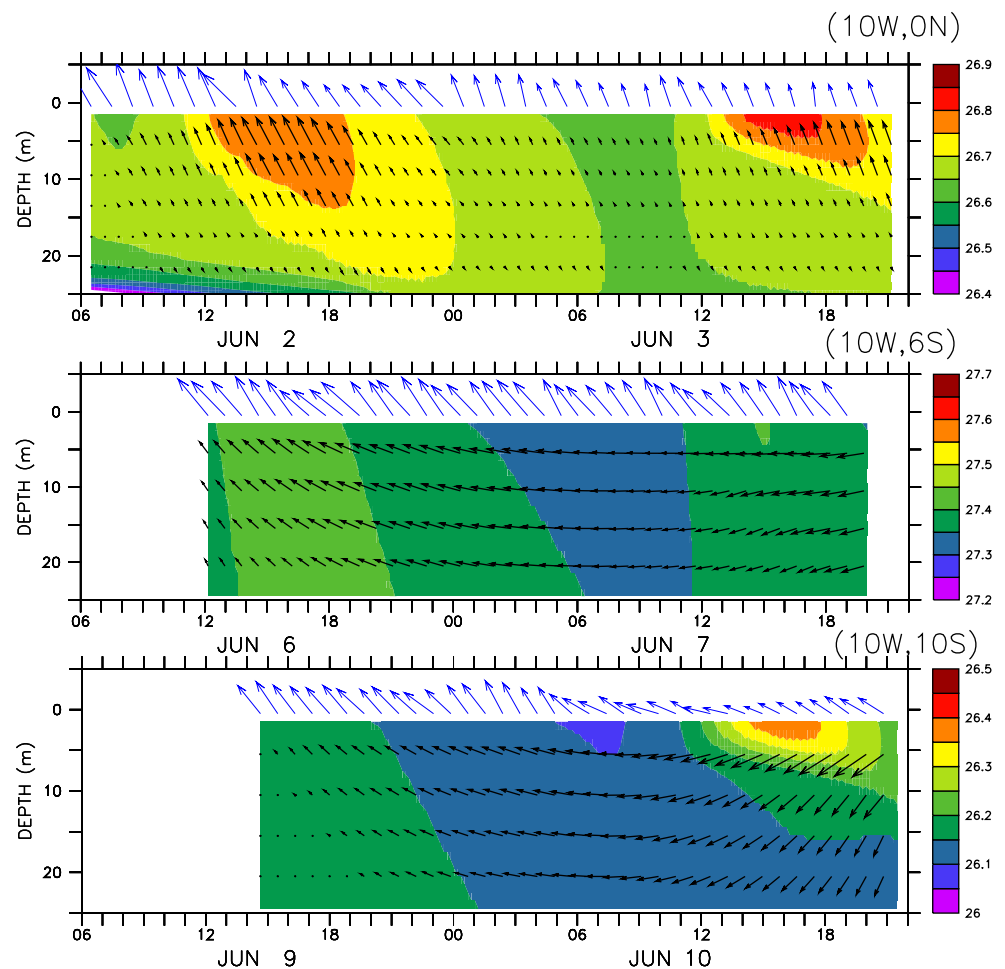
diurnal cycle; the maximum amplitude of the diurnal cycle occurs at a depth between the surface and the nocturnal MLD.

At 6° S, both observed and simulated dissipation rates reveal low values of dissipation $<10^{-9}$ Wkg^{-1} inside the mixed layer (Fig. 11). On the other hand, at 0° N and 10° S, dissipation $<10^{-9}$ Wkg^{-1} occurs below the mixed layer. This occurrence is unique and due to the absence of noticeable restratification during the course of the day. Note also that at the other locations, a rather good correspondence exists between the MLD defined with the temperature criterion adopted here and low values of TKE dissipation rates.

Meanwhile, observations reveal the presence of some intermittent patches of high dissipation rates below the MLD (i.e., at 0° N on June 2 and between 0800 and 1100 UTC on June 3 and at 6° S below 70-m depth) that are not present in the simulation, where turbulence dissipation rates below the MLD remain nearly constant. In the EEA, elevated mixing levels in the upper shear zone of the EUC have been observed (Crawford and Osborn 1979). Intermittent patches of dissipations in the microstructure measurements reveal that high mixing below the MLD is not solely due to shear production or nighttime

cooling but probably to other mixing processes, such as internal waves breaking as pointed out by Moum et al. (1992). Discrepancies of turbulent dissipation rates between the model and the observation, especially at 0° N, suggest that shear production in the thermocline is underestimated by the model.

At stations, during the diurnal stratification period (1200–1600 UTC), turbulence just below the MLD is weak, with values ranging from 10^{-9} to 10^{-10} Wkg^{-1} showing that the water column is highly stable at this time, thus preventing any TKE generation and dissipation.

It is also interesting to note the asymmetry between the rapid decrease of dissipation propagating upward during the restratification period and the slower downward increase of dissipation during the nocturnal convection period. On the other hand, the diurnal cycle of turbulence dissipation is more pronounced at 6° S than at 0° N and 10° S, a feature reflecting the presence of stronger winds, mixing, and dissipation at this station.

Similar results have been obtained in the tropical Pacific basin with various one-dimensional models and have been compared successfully with observed dissipation rates during dedicated experiments like the Tropical Heat 1984
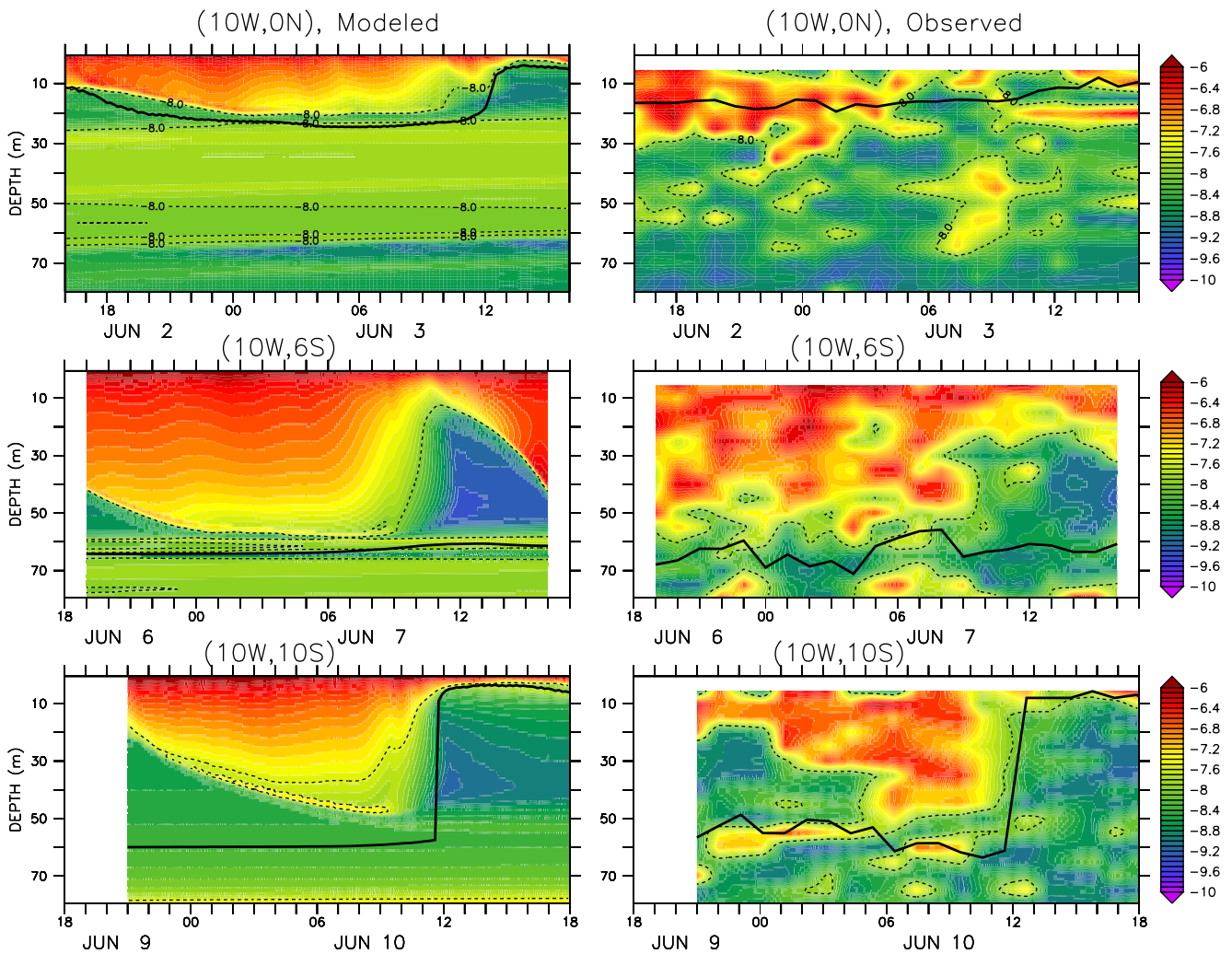
Fig. 11 Time series of vertical profiles of turbulence dissipation ($Log_{10}\varepsilon$) at $0°$ N (*top*); $6°$ S (*middle*), and $10°$ S (*bottom*, Wkg^{-1}). The mixed layer depth is indicated (*full line*) as is the isoline -8 (*dashed*)

by Moum and Caldwell (1985) and Gregg et al. (1985) and the Tropical Heat 1987 by Moum et al. (1992) and Hebert et al. (1991), or TOGA-COARE by Clayson and Kantha (1999).

3.6 Heat budget

The time series of the different terms of Eq. 17 are presented in Fig. 12, over a full day starting at 1900 UTC. For clarity, a smoothing filter has been applied to each term of the budget to filter out small variations for clarity. At each station, the heat storage term experiences a clear diurnal cycle, reflecting the diurnal cycle of the net heat flux, in agreement with Fig. 5. It consists in a heat loss during the night and in a heat gain during the day from 0800–0900 UTC to 1600–1700 UTC. At the three stations, heat gain is solely supplied by the net short-wave radiation except at $0°$ N, where the vertical diffusion of heat at the

MLD base displays a weak heat gain to the budget between 0400 and 0800 UTC.

However, the importance of the other terms in the heat budget varies at the three stations. On average, the vertical diffusion of heat at the mixed-layer base contributes largely to the cooling of the mixed layer, with a diurnal minimum between 1200 and 1500 UTC of -200 Wm^{-2} at $0°$ N and -300 Wm^{-2} at $10°$ S. The diurnal cycle of this term comes from the existence of the diurnal stratification generated by the net solar radiation. Vertical diffusion then tends to cool and erode the base of this stratification as soon as it appears. On the other hand, the vertical diffusion at $6°$ S does not significantly contribute to the heat budget because of the absence of diurnal stratification.

The contribution of entrainment to the heat budget is significantly important only at the equator where it cools the mixed layer continuously at a rate of about -100 Wm^{-2}, a process expected at this period corresponding

Fig. 12 Heat budget (Wm^{-2}) over 24 h as a function of time at 0° N (*top*), 6° S (*middle*), and 10° S (*bottom*). Tendency is in *black*; solar heat flux in *red*; turbulent surface heat flux in *green*; vertical entrainment in *blue*; and vertical turbulent diffusion in *cyan*
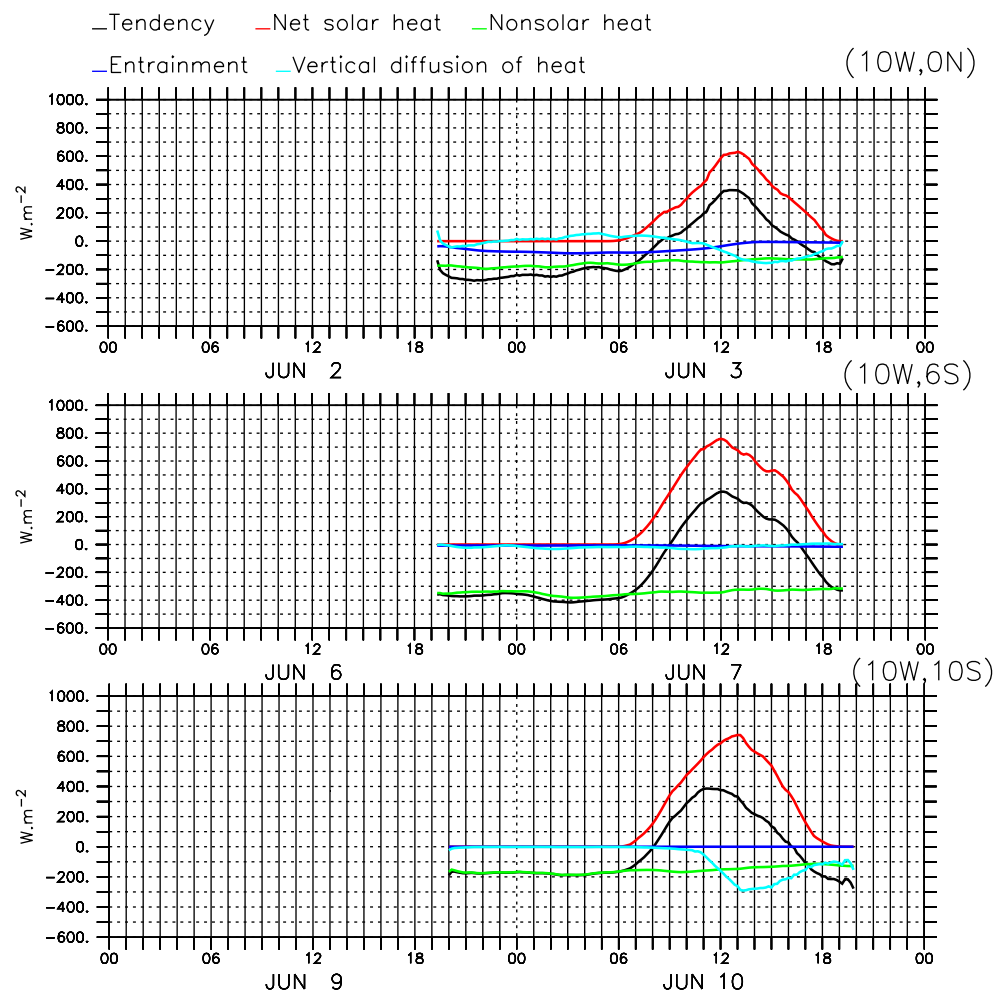
to ACT development. Note that during the afternoon, the contribution of entrainment is reduced. This is because the vertical gradient of temperature is weaker at the base of the diurnal inversion than at the base of the nocturnal mixed layer.

3.7 TKE budget

Figure 13 shows the time variation of each term of Eq. 18. The magnitude of the different terms of the budget at 6° S is nearly fourfold greater than at 0° N and 10° S. This is a consequence of the combined effect of stronger winds and a global negative heat budget.

At all stations, there is a clear night–day difference in the budget. During the night, the buoyancy production term dominates the supply of TKE at 6° S and 10° S. At 0° N, this term remains important, but is weaker than the shear production term due to the presence of the sheared current system (EUC and SEC). During this period, the dissipation is strongly negative.

During the day, the buoyancy production diminishes just after sunrise and remains constant at nearly zero

between noon and 1800 UTC. Each TKE production term is weaker compared to its nocturnal value and the dissipation increases toward zero. Due to the extinction of buoyancy production during the day, the budget of TKE is practically governed by the balance between shear production, vertical diffusion and dissipation because as expected, the tendency term remains close to zero during all the simulations.

Moreover, in the three simulations, we observe that: (1) the nocturnal buoyancy production is always a source of TKE—this results from the nocturnal convection during which the negative surface heat flux destabilizes the upper mixed layer; (2) the shear production is maximum at night and diminishes when the sun rises; and (3) the vertical diffusion term is a source of TKE and helps to increase mixing at these stations.

4 Conclusion

In this study, a one-dimensional model is used to simulate the diurnal cycle of the mixed layers during the EGEE-3

Fig. 13 Turbulent kinetic energy budget ($\times 10^{-6}$ m^{3}s^{-3}) over 24 h as a function of time at 0° N (*top*), 6° S (*middle*), and 10° S (*bottom*). Tendency in *black*; buoyancy production in *red*; shear production in *green*; dissipation in *blue*; and vertical diffusion in *cyan*. Note the scale at 6° S is roughly two times greater than that at 0° N and 10° S
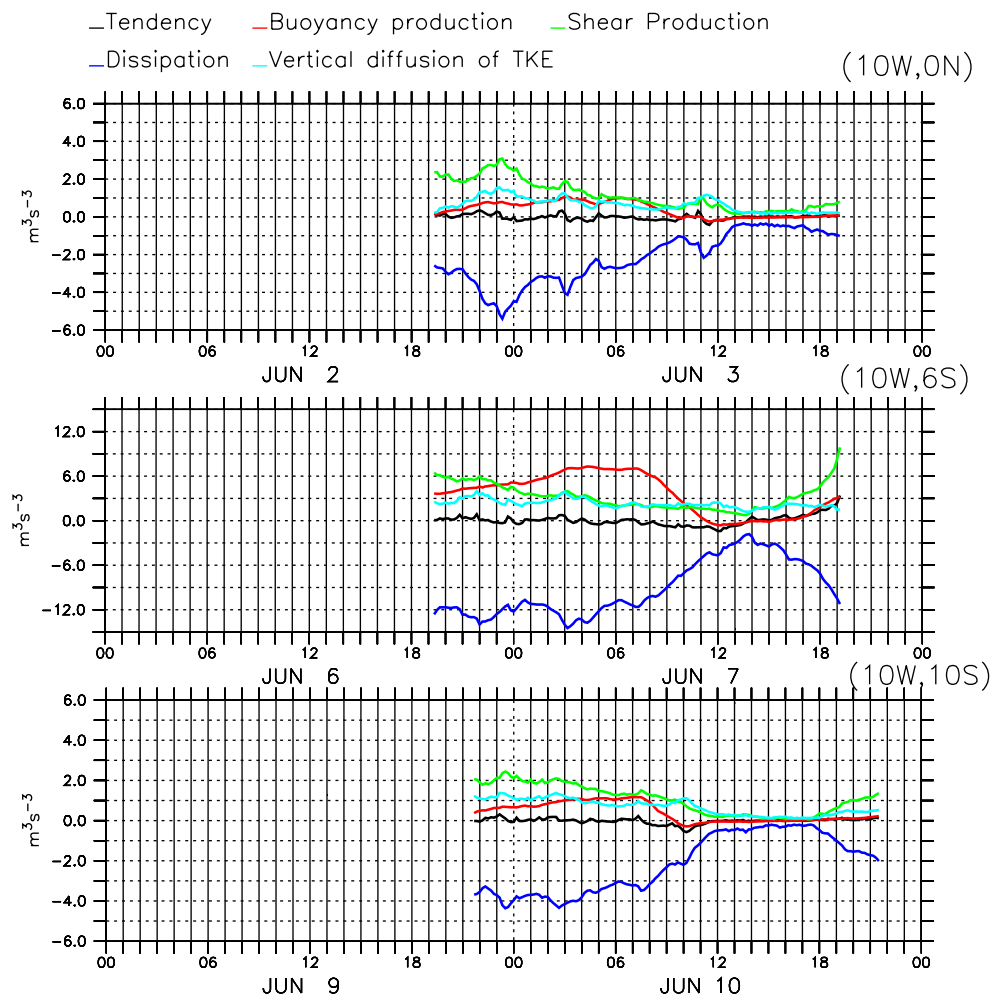
campaign (June 2006). Mixed-layer diurnal processes at three PIRATA mooring locations of the eastern equatorial Atlantic (10° W–0° N; 10° W–6° S; 10° W–10° S) are simulated over the 1 or 2 days they were visited. These locations experienced different meteorological conditions, thus allowing us to identify the different mechanisms of diurnal variability in various meteorological and oceanic conditions.

Our results show that the variability of the SST is quite well simulated when compared with independent observations. Moreover, the realism of the simulations is mainly due to the high quality of the surface fluxes used to force the model and to the initialization of the model with observed temperature and salinity profiles.

The diurnal response of the near-surface temperature to daytime heating and nighttime cooling was found to have an amplitude of a few tenths of a degree Celsius. Observed and simulated mixed-layer thickness show that the MLD can vary by several tens of meters in a diurnal cycle (i.e., from 60 to <10 m at 10° S (Fig. 9) or from 20 to 5 m at 0° N). On the other hand, intense mixing due to the strengthening of the southeastern trades can suppress the diurnal variation of

the MLD (at 6° S), without, however, affecting the depth of the permanent thermocline.

These observations confirm that the existence or absence of any diurnal variation of MLDs does not seem to affect the thermocline depth, meaning that this relatively stable feature of the EEA does not mainly result from the surface fluxes but would also be due to the larger scale effect of the circulation as suggested by Provost et al. (2006) and Giordani and Caniaux (2010).

The mixed layer gains heat through the net solar radiation and loses heat through the non-solar heat fluxes and at a lower level to vertical diffusion. The peak of the heat gain is nearly 400 W m^{-2} and occurs around 1400 UTC when the net solar radiation is maximum. The vertical diffusion of heat cools the diurnal mixed-layer base at a maximum rate of 200 and 300 W m^{-2} at 0° N and 10° S, respectively, when a well-established diurnal stratification exists in the first few meters near the surface, between 1300 and 1500 UTC. This process is negligible at 6° S because stronger winds prevailed when the buoy was visited, thus preventing any diurnal stratification. The contribution of entrainment to the heat balance is significant only at the

equator, where it cools the mixed layer with a maximum rate of nearly 100 W m^{-2}.

Comparisons of the simulated turbulence dissipation with independent observations (microstructure measurements) at different locations of the eastern equatorial Atlantic reveal that the model simulates the turbulence and its diurnal cycle reasonably well. As in the observations, the modeled turbulence appears to be mainly confined inside the mixed layer at 0° N and 10° S. Both the magnitude and the variability of the turbulence cycle are reasonably well simulated, suggesting that the one half turbulence closure is sufficient to capture the main turbulence cycle in the mixed layer. However, our simulations do not indicate the presence of strong bursts of turbulence penetrating well below the mixed layer as observed in the microstructure data. These strong and intermittent patches of dissipations observed early on in the Pacific by Clayson and Kantha (1999) and Moum et al. (1992) were attributed to the vertical shear of current (Clayson and Kantha 1999) and to internal waves breaking (Moum et al. 1992). The lack of strong and intermittent patches of dissipation rates in the thermocline in our simulation suggests that turbulence is not well resolved at these levels. However, the main futures of turbulence dissipation are captured by the model inside the mixed layer.

The TKE budget shows that all terms of the TKE equation contribute to the mixing processes but the buoyancy production term is dominant, especially during the night and, to a lesser degree, through shear production and vertical diffusion. At 6° S, the higher wind stress considerably increased the TKE budget compared to the other stations, with a high production rate due to buoyancy, shear, and vertical diffusion.

In the tropic, the ocean diurnal warming can induce an increase in the net surface heat flux toward the atmosphere of 50 W m^{-2} during the day, under clear sky and calm conditions (Fairall et al. 1996; Ward 2006). Hence, the ocean diurnal cycle can feedback onto the atmosphere and take part in the atmosphere–ocean coupling mechanisms. For instance, the SST diurnal variations can affect the life cycle of tropical convective clouds (Chen and Houze 1997; Woolnough et al. 2000; Dai and Trenberth 2004) and the atmospheric profiles of heat, moisture, and cloud properties (Clayson and Chen 2002). Furthermore, recent studies suggest that resolving the SST variability on diurnal timescales can significantly modulate the amplitude of SST variability on seasonal timescales (Shinoda and Hendon 1998; Bernie et al. 2005, 2007; Shinoda 2005; Bellanger 2007) or even longer timescales (Danabasoglu et al. 2006) and improve the representation of ocean–atmosphere coupled modes of variability, such as the Madden–Julian Oscillation (Bernie et al. 2005, 2008), the phase of the Madden–Julian Oscillation (Woolnough et al. 2007). In our study, computing the mixed-layer heat budget as on Fig. 12, but using daily

mean surface fluxes, leads to a rectification process on the tendency term of ~50 W m^{-2} at 0° N and 15 W m^{-2} at 10° S. At 6° S, this term is not noticeable. However, our calculation was performed on a too short period (two diurnal cycles) to strongly conclude. But all these findings support the idea that the parameterization of diurnal cycle may help in improving the realism of general circulation models

References

Adamec D, O'Brien JJ (1978) The seasonal upwelling in the Gulf of Guinea due to remote forcing. J Phys Oceanogr 8:1050–1060

Anderson RJ (1993) A study of wind stress and heat flux over the open ocean by the inertial dissipation method. J Phys Oceanogr 23:2153–2161

Bellanger H (2007) Rôle de l'interaction océan-atmosphère dans la variabilité intrasaisonnière de la convection tropicale. PhD thesis, Ecole Polytechnique

Bernie DJ, Woolnough SJ, Slingo JM, Guilyardi E (2005) Modeling diurnal and intraseasonal variability of the ocean mixed layer. J Climate 18:1190–1202

Bernie DJ, Guilyardi E, Madec G, Slingo JM, Woolnough SJ (2007) Impact of resolving the diurnal cycle in an ocean–atmosphere GCM: part I: diurnally forced OGCM. Clim Dyn 29:575–590

Bernie DJ, Guilyardi E, Madec G, Slingo JM, Woolnough SJ, Cole J (2008) Impact of resolving the diurnal cycle in an ocean–atmosphere GCM: part 2: a diurnally coupled OGCM. Clim Dyn 31:909–925

Bougeault P, Lacarrère P (1989) Parameterization of orography-induced turbulence in a meso-beta-scale model. Mon Weather Rev 117:1872–1890

Bourlès B, Gouriou Y, Chuchla R (1999) On the circulation and upper layer of the western equatorial Atlantic. J Geophys Res 104 (C9):21151–21170

Bourlès B, D'Orgeville M, Eldin G, Chuchla R, Gouriou Y, du Penhoat Y, Arnault S (2002) On the thermocline and subthermocline eastward currents evolution in the eastern equatorial Atlantic. Geophys Res Lett 29(16):32.1–32.4. doi:10.1029/2002GL015098

Bourlès B, Brandt P, Caniaux G, Dengler M, Gouriou Y, Key E, Lumpkin R, Marin F, Molinari RL, Schmid C (2007) African Monsoon Multidisciplinary Analysis (AMMA): special measurements in the tropical Atlantic. CLIVAR Newsl Exchanges 41(12):7–9

Bourlès B, Busalacchi AJ, Campos E, Hernandez F, Lumpkin R, McPhaden MJ, Moura AD, Nobre P, Planton S, Servain J, Trotte J, Yu L (2008) The PIRATA program: history and accomplishments of the 10 first years tropical Atlantic observing system's backbone. Bull Am Meteorol Soc 89(8):1111–1125. doi:10.1175/2008BAMS2462.1

Bourras D, Weill A, Caniaux G, Eymard L, Bourlès B, Letourneur S, Legain D, Key E, Baudin F, Piguet B, Traullé O, Bouhours G, Sinardet B, Barrié J, Vinson JP, Boutet F, Berthod C, Clémençon A (2009) Turbulent air–sea fluxes in the Gulf of Guinea during the AMMA experiment. J Geophys Res 114:C04014. doi:10.1029/2008JC004951

Bunge L, Provost C, Kartavtseff A (2007) Variability in horizontal current velocities in the central and eastern equatorial Atlantic in 2002. J Geophys Res 112:C02014. doi:10.1029/2006JC003704

Caniaux G, Planton S (1998) A three-dimensional ocean mesoscale simulation using data from the SEMAPHORE experiment: mixed layer heat budget. J Geophys Res 103(C11):25081–25099

Caniaux G, Giordani H, Redelsperger JL, Guichard F, Key E, Wade M (2010) Coupling between the Atlantic cold tongue and the African monsoon in boreal spring and summer. Submitted to JGR

Carton JA, Zhou ZX (1997) Annual cycle of sea surface temperature in the tropical Atlantic Ocean. J Geophys Res 102:27813–27824

Chen SS, Houze RA (1997) Diurnal variation and life-cycle of deep convective systems over the tropical Pacific warm pool. Quart J Roy Meteor Soc 123:357–388

Clayson CA, Chen A (2002) Sensitivity of a coupled single-column model in the tropics to treatment of the interfacial parameterizations. J Clim 15:1805–1831

Clayson CA, Kantha LH (1999) Turbulent kinetic energy and its dissipation rate in the equatorial mixed layer. J Phys Oceanogr 29:2146–2166

Crawford WR, Osborn TR (1979) Microstructure measurements in the Atlantic equatorial undercurrent during GATE. Deep Sea Res II 6:285–308

Cronin MF, Kessler WS (2009) Near-surface shear flow in the tropical Pacific cold tongue front. J Phys Oceanogr 39:1200–1215

Cronin MF, McPhaden MJ (1997) The upper ocean heat balance in the western equatorial Pacific warm pool during September–December 1992. J Geophys Res 102:8533–8553

Dai A, Trenberth KE (2004) The diurnal cycle and its depiction in the community climate system model. J Clim 17:930–951

Danabasoglu G, Large W, Tribbia J, Gent P, Briegleb B (2006) Diurnal coupling in the tropical oceans of CCSM3. J Climate 19:2347–2365

DeCosmo J, Katsaros KB, Smith SD, Anderson RJ, Oost WA, Bumke K, Chadwick H (1996) Air–sea exchange of water vapor and sensible heat: The Humidity Exchange Over the Sea (HEXOS) results. J Geophys Res 101:12001–12016

Dengler M, Bourlès B, Chuchla R, Toole J (2010) Enhanced upper ocean mixing and turbulent heat flux in the equatorial Atlantic at 10°W. Geophys Res Lett (in press)

Dourado MS, Caniaux G (2004) One-dimensional modeling of the oceanic boundary layer with PIARATA data at 10°S 10°W. Rev Brasilieria Meteorologia 19(2):217–226

Fairall CW, Bradley EF, Godfrey JS, Wick GA, Edson JB (1996) Cool-skin and warm-layer effects on sea surface temperature. J Geophys Res 101:1295–1308

Fairall CW, Bradley EF, Hare JE, Grachev AA, Edson JB (2003) Bulk parameterization of air–sea fluxes: updates and verification for the COARE algorithm. J Clim 16:571–591

Foltz G, Grodsky SA, Carton JA, McPhaden MJ (2003) Seasonal mixed layer heat budget of the tropical Atlantic Ocean. J Geophys Res 108(C5):3146–3159. doi:10.1029/2002JC001584

Gaspar P, Gregoris Y, Lefevre JM (1990) A simple eddy kinetic energy model for simulations of the oceanic vertical mixing: tests at station PAPA and Long-Term Upper Ocean Study site. J Geophys Res 95:16179–16193

Giordani H, Caniaux G (2010) Diagnosing vertical motion at the equatorial Atlantic. Submitted to JGR

Gregg MC, Peters H, Wesson JC, Oakey NS, Shay TJ (1985) Intensive measurements of turbulence and shear in the equatorial undercurrent. Nature 318:140–144

Hebert D, Moum JN, Caldwell DR (1991) Does ocean turbulence peak at the Equator? Revisited. J Phys Oceanogr 21:1690–1698

Hormann V, Brandt P (2007) Atlantic equatorial undercurrent and associated cold tongue variability. J Geophys Res 112:C06017. doi:10.1029/2006JC003931

Janicot A, Ali A, Asencio N, Berry G, Bock O, Bourles B, Caniaux G, Chauvin F, Deme A, Kergoat L, Lafore JP, Lavaysse C, Lebel T, Marticorena B, Mounier F, Nedelec P, Redelsperger JL, Ravegnani F, Reeves CE, Roca R, de Rosnay P, Schlager H, Sultan B, Thorncroft C, Tomasini M, Ulanovsky A, ACMAD forecasters team (2008) Large-scale overview of the summer monsoon over West and Central Africa during the AMMA field experiment in 2006. Ann Geophys 26:2569–2595

Jerlov NG (1968) Optical oceanography. Elsevier, Amsterdam, 194 pp

Josse P (1999) Modélisation couplée ocean–atmosphère à mésoéchelle: application à la campagne SEMAPHORE. Toulouse. PhD thesis, Université Paul Sabatier (available in French at CNRM)

Kantha LH, Clayson CA (1994) An improved mixed layer model for geophysical applications. J Geophys Res 99:25235–25266

Kolmogorov AN (1942) Equations of turbulent motion of an incompressible fluid. Izvestia Acad Sci USSR Phys 6:56–58

Kolodziejczyk N, Bourlès B, Marin F, Grelet J, Chuchla R (2009) Seasonal variability of the equatorial undercurrent at 10°W as inferred from recent in situ observations. J Geophys Res 114: C06014.1–C06014.16. doi:1029/2008JC004976

Large WG, McWilliams JC, Doney SC (1994) Oceanic vertical mixing: a review and a model with a nonlocal boundary layer parameterization. Rev Geophys 32:363–403

Leduc-Leballeur M, Eymard L, de Coetlogon G (2010) Observation of the marine atmospheric boundary layer in the gulf of Guinea during the 2006 boreal spring. Submitted to QJRMS

Lefèvre N, Guillot A, Beaumont L, Danguy T (2008) Variability of fCO$_2$ in the eastern tropical Atlantic from a moored buoy. J Geophys Res 113:C01015. doi:10.1029/2007JC004146

Marin F, Caniaux G, Bourlès B, Giordani H, Gouriou Y, Key E (2009) Why were sea surface temperatures so different in the eastern equatorial Atlantic in June 2005 and 2006? J Phys Oceanogr 39:1416–1431

McCreary J, Picaut J, Moore D (1984) Effects of the remote annual forcing in the eastern tropical Atlantic Ocean. J Mar Res 42(45):81

Merle J, Fieux M, Hisard P (1980) Annual signal and interannual anomalies of sea surface temperature in the eastern equatorial Atlantic. Deep Sea Res 26 GATE Suppl, pp 77–101

Mignot J, de Boyer Montégut C, Lazar A, Cravatte S (2007) Control of salinity on the mixed layer depth in the world ocean. Part II: tropical and subtropical areas. J Geophys Res 112:C10010. doi:10.1029/2006JC003954

Moore DW, Hisard P, McCreary JP, Merle J, O'Brien JJ, Picaut J, Verstraete JM, Wunsch C (1978) Equatorial adjustment in the eastern Atlantic. Geophys Res Lett 5:311–348

Moum JN, Caldwell DR (1985) Local influences on shear flow turbulence in the equatorial ocean. Science 230:315–316

Moum JN, Hebert D, Paulson CA, Caldwell DR (1992) Turbulence and internal waves at the Equator. Part I: statistics from towed thermistors and a microstructure profiler. J Phys Oceanogr 22:1330–1345

Pailler K, Bourlès B, Gouriou Y (1999) The barrier layer in the western Atlantic Ocean. Geophys Res Lett 26:2069–2072

Paulson CA, Simpson JJ (1977) Irradiance measurements in the upper ocean. J Phys Oceanogr 7:952–967

Persson POG, Hare JE, Fairall CW, Otto WD (2005) Air–sea interaction processes in warm and cold sectors of extratropical cyclonic storms observed during FASTEX. Q J R Meteorol Soc 131:877–912

Peter AC, Le Henaff M, du Penhoat Y, Menkes CE, Marin F, Vialard J, Caniaux G, Lazar A (2006) A model study of the seasonal mixed layer heat budget in the equatorial Atlantic. J Geophys Res 111:C06014. doi:10.1029/2005JC003157

Philander SG (1990) El Niño, La Niña and the Southern Oscillation. Academic, San Diego, 286 pp

Philander SG, Pacanowski RC (1986) A model of the seasonal cycle in the tropical Atlantic Ocean. J Geophys Res 91 (C12):14192–14206

Picaut J (1983) Propagation of the seasonal upwelling in the eastern equatorial Atlantic. J Phys Oceanogr 13:18–37

Prandke H, Stips A (1998) Test measurements with an operational microstructure-turbulence profiler: detection limit of dissipation rates. Aquat Sci 60:191–209

Provost C, Chouaib N, Spadone A, Bunge L, Arnault S, Sultan E (2006) Interannual variability of the zonal sea surface slope at the equator in the Atlantic in the 1990's. J Adv Space Res 37:823–831

Redelsperger JL, Thorncroft CD, Diedhiou A, Lebel T, Parker DJ, Polcher J (2006) African monsoon multidisciplinary analysis: an International Research Project and Field Campaign. Bul Amer Meteorol Soc 87:1739–1746

Schmitt RW, Ledwell JR, Montgomery ET, Polzin KL, Toole JM (2005) Enhanced diapycnal mixing by salt fingers in the thermocline of the tropical Atlantic. Science 308:685–688

Schudlich RR, Price JF (1986) Diurnal cycles of current, temperature, and turbulent dissipation in a model of the equatorial upper ocean. J Geophys Res 97:5409–5422

Shinoda T (2005) Impact of diurnal cycle of solar radiation on intraseasonal SST variability in the western equatorial Pacific. J Clim 18:2628–2636

Shinoda T, Hendon HH (1998) Mixed layer modeling of intraseasonal variability in the tropical western Pacific and Indian oceans. J Clim 11:2668–2685

Smith SD (1980) Wind stress and heat flux over the ocean in gale force winds. J Phys Oceanogr 10:709–726

Sprintall J, McPhaden MJ (1994) Surface layer variations observed in multiyear time series measurements from the western equatorial Pacific. J Geophys Res 99:963–979

Stramma L, Schott F (1999) The mean flow field of the tropical Atlantic Ocean. Deep Sea Res II 4:279–304

Stramma L, Fischer J, Brandt P, Schott F (2003) Circulation, variability and near equatorial meridional flow in the central tropical Atlantic. Interhemispheric water exchange in the Atlantic Ocean. Elsevier Oceanogr Ser 68:1–22

Takahashi T, Sutherland SC, Wanninkhof R, Sweeney C, Feely RA, Chipman DW, Hales B, Friederich G, Chavez F, Watson A, Bakker DCE, Schuster U, Metzl N, Yoshikawa-Inoue H, Ishii M, Midorikawa T, Nojiri Y, Sabine C, Olafsson J, Arnarson TS, Tilbrook B, Johannessen T, Olsen A, Bellerby R, Körtzinger A, Steinhoff T, Hoppema M, de Baar MJW, Wong CS, Delille B, Bates NR (2009) Climatological mean and decadal changes in surface ocean pCO_2, and net sea–air CO_2 flux over the global oceans. Deep Sea Res II 56:554–577

Taylor KE (2001) Summarizing multiple aspects of model performance in a single diagram. J Geophys Res 106(D7):7183–7192

Voituriez B, Herbland A (1977) Étude de la production pélagique de la zone équatoriale de l'Atlantique a 4°W. I. Relation entre la structure hydrologique et la production primaire. Cah O.R.S.T.O.M. Sér Oceanogr 15:313–331

Ward B (2006) Near-surface ocean temperature. J Geophys Res 111: C02004. doi:10.1029/2004JC002689

Weill A, Eymard L, Caniaux G, Hauser D, Planton S, Dupuis H, Brut A, Guérin C, Nacass P, Butet A, Cloché S, Pedreros R, Durand P, Bourras D, Giordani H, Lachaud G, Bohours G (2003) Determination of turbulent air–sea fluxes from various mesoscale experiments: a new perspective. J Clim 16(4):600–618

Woolnough SJ, Slingo JM, Hoskins BJ (2000) The relationship between convection and sea surface temperature on intraseasonal timescales. J Climate 13:2086–2104

Woolnough SJ, Vitart F, Balmaseda MA (2007) The role of the ocean in the Madden–Julian Oscillation: implications for MJO prediction. Quart J Roy Meteor Soc 133:117–128

Yu L, Jin X, Weller RA (2006) Role of net surface heat flux in the seasonal evolution of sea surface temperature in the Atlantic Ocean. J Clim 19:6153–6169